Detonation in Hydrogen-Nitrous Oxide-Diluent Mixtures: An Experimental and Numerical Study

R. Mével[a,b,c], D. Davidenko[b], F. Lafosse[b], N. Chaumeix[b], G. Dupré[b,c], C.-E. Paillard[b,c], J.E. Shepherd[a]

[a] *Graduate Aeronautical Laboratories, California Institute of Technology, Pasadena, USA*
[b] *Institut de Combustion, Aérothermique, Réactivité et Environnement, Orléans, France*
[c] *University of Orléans, Department of Chemistry, Orléans, France*

Abstract

Knowledge of H_2-N_2O mixtures explosive properties is important to the safety of nuclear waste storage and semi-conductor manufacturing processes. The present study provides new experimental data on H_2-N_2O detonations, and proposes a thermochemical model which is used to numerically simulate detonation propagation. Detonation cell size has been measured in a variety of H_2-N_2O-Ar mixtures. Even at low initial pressure, these mixtures are very sensitive to detonation with cell size of few millimeters. Using a reduced version of a detailed reaction scheme, 2-D Euler simulations have been used to examine the features of detonation in H_2-N_2O-Diluent mixtures. A PLIF model has been applied to allow for direct comparison with experimental results. Statistical analysis of the cellular cycle dynamics has been performed.

Key words: Detonation structure, Cell size, Reduced kinetics, 2-D simulation, Hydrogen, Nitrous oxide, Laser induced fluorescence

PACS: 01.50.Kw, 47.15.Pn, 47.40.Rs

*Corresponding author: mevel@caltech.edu

1. Introduction

Hydrogen-nitrous oxide chemistry plays an important role in the analysis of potential hazards in the storage and processing of high-level radioactive waste [1]. It is also important for silane oxidation by nitrous oxide [2, 3] because the thermal decomposition of silane is faster than that of nitrous oxide and results in the release of molecular hydrogen [4]. Silane-nitrous oxide mixtures are widely used in the semi-conductor industry [5] in order to form insulator or protective layers [6, 7, 8, 9] in a wide variety of applications [10, 11, 12]. These mixtures have been involved in some accidental combustion events [13].

Among possible combustion events, detonation is the most severe and has the greatest potential for structural damage. Although direct initiation of detonation is usually considered unlikely, studies have shown that confinement and congestion can lead to detonation initiation via the deflagration-to-detonation transition (DDT) process [14]. The estimation of detonation properties, particularly cell size, is of fundamental importance for evaluation of detonation hazards in industrial processes.

Previous studies on hydrogen-nitrous oxide mixtures have generated data sets on the ignition delay time [15, 16, 17, 18, 19, 20, 21, 22, 23, 24, 25, 26], the laminar burning speed [27, 28, 29, 30, 31, 32, 33, 34, 35], and the minimum ignition energy [36]. Concerning detonation, Zhang et al measured the critical energy for direct initiation [37] and the cell sizes have been measured [38, 39] in the frame work of nuclear waste storage risk assessment. Although effects of equivalence ratio, initial pressure and dilution have been extensively studied, the available data on the cell size are limited compared

to hydrocarbon-air or hydrogen-air mixtures.

The objectives of the present study are: to provide additional experimental data on the detonation cell size in hydrogen-nitrous oxide mixtures; to propose a realistic chemical reaction model validated against shock tube and flow reactor studies; and to carry out numerical simulations of detonation front structure based on a reduced version of the reaction model.

2. Materials and methods

2.1. Experimental set-up

Hydrogen-nitrous oxide-argon mixtures were prepared from high purity grade gases supplied by Air Liquide. Each gas was introduced in a 10 L glass tank using the partial pressure method and mixed by a magnetic stirrer for at least half an hour prior to experiments. The initial conditions were varied within the following ranges: equivalence ratio, Φ, between 0.3 and 2.5; dilution from 20 to 60 mol% of Ar; initial pressure between 7 and 35 kPa; and initial temperature of 295 K. Detonations were initiated by incident shock waves using a shock-tube. The shock tube is made of stainless steel with a driver section of 0.9 m long and with an inner diameter of 128 mm. The driven section is either 3.8 or 4.6 m long and has an inner diameter of 78 mm. The two parts of the tube are linked to two vacuum pumps and separated by a double membrane system which allows a good control of the driver section pressure, P_4. Four pressure transducers are mounted flush to the driven section inner wall and allow to measure the shock velocity with an accuracy of 1%. The measured velocity is then used to calculate the temperature and

pressure conditions behind the shock wave. The soot record method was used to determine the detonation cell size. The soot foils were located at the end of the driven section. Soot records were digitised and analysed using the Visilog software.

2.2. Kinetic modeling

The chemical kinetic model used in the present study consists of 203 reactions and 32 species [24, 3]. It was mainly based on the Konnov [40] and Mueller et al. [41] mechanisms. The rate constant for the N_2O decomposition reaction was taken from Javoy et al. study [25]. A kinetic sub-set for excited OH radical, OH*, was based on the mechanisms of Hidaka et al. [21] and Hall and Petersen [42, 43]. All thermodynamic data were taken from the Konnov and Mueller et al. models except those for OH*, which were from Hall and Petersen. Shock tube and flow reactor experiments were both modeled using the SENKIN code [44] from the CHEMKIN II package. Constant volume and constant pressure adiabatic reactor models were chosen to model the experimental conditions of shock tube and flow reactor tests, respectively. For the flow reactor data set, the time-shifting method was used as described by Yetter et al. [45]. Sensitivity and reaction pathway analysis were also performed using the SENKIN code.

2.3. Kinetic scheme reduction

The detailed kinetic model is too large to be directly applied to multidimensional detonation simulations. To allow simulations with the 2-D Euler code described below, the kinetic scheme must be reduced to the minimum number of reactions describing the heat release dynamics in the detonation

wave.

The reduction was conducted using an automatic procedure [46] for the elimination of redundant chemical reactions. This procedure performs simulations of an autoignition process in a homogeneous adiabatic constant-pressure reactor using a code analogous to SENKIN. The reaction importance is evaluated from an error criterion based on the following macroscopic characteristics of the oxidation process: ignition delay time (time to the thermicity peak), maximum thermicity, profiles of temperature and mixture molar mass. The errors are determined with respect to the same characteristics obtained with the detailed kinetic model. Reactions are eliminated one after another starting from the least important one until none of the remaining reactions can be deleted without exceeding the imposed error tolerances. The following error tolerances are chosen for the reduction: 10% for the ignition delay time, 10% for the maximum thermicity, 150 K for the temperature profile, 50 K for the temperature at equilibrium, 5% for the molar mass profile, and 2% for the molar mass at equilibrium. Table 1 summarizes the error criteria used for the reduction and the corresponding error tolerances. The reduction is made locally, that is for fixed mixture composition, initial pressure and temperature. To obtain a reduced kinetic scheme that is valid for a certain range of initial conditions, the local reduction is performed at several conditions specified in terms of pressure and temperature. Then the locally-obtained reduced mechanisms are merged in a single overall reduced mechanism, which is then tested over the whole range of initial conditions to verify the error tolerances.

2.4. Numerical simulations

Detonation propagation in a planar 2-D geometry was simulated numerically using an inviscid (Euler) model for compressible reacting flow. The numerical method is based on the shock-capturing, weighted essentially non-oscillatory (WENO) scheme of the fifth order [47]. To minimize restrictions on the time step resulting from the stiff chemical source terms, which can be prohibitive at triple points, the time integration is performed with the semi-implicit additive Runge-Kutta scheme ASIRK2C [48]. The convective terms are included in the explicit operator whereas all the source terms are treated implicitly. The fluid dynamic time step is controlled by a constant Courant number of 0.7. The code is parallized using the MPI library.

Simulations were performed on two rectangular domains whose dimensions are 150 mm in the direction of detonation propagation and 39 mm or 78 mm in the transverse direction. The latter corresponds to the detonation tube diameter. The computational mesh is structured and orthogonal. In the longitudinal direction, it consists of 500 points uniformly distributed with a spacing of 25, 50 or 100 μm followed by 500 points with progressively increasing spacing. Considering the distance to maximum thermicity as a characteristic chemical length, the number of grid points per length scale ranges between 13 and 66 depending on the mixture. The detonation front is always captured within the first mesh portion. In the transverse direction, the mesh consists of 400 or 800 equally spaced points.

To obtain a mean stationary detonation front, a uniform flow at the Chapman-Jouguet (CJ) detonation velocity is imposed at the inlet boundary. The conditions on the outlet boundary are obtained by solving a local Riemann

problem between the state at the last internal grid point and the CJ state. Symmetry conditions are imposed on the two lateral boundaries.

The 2-D solution is initialized from a 1-D solution for a slightly overdriven detonation. The inflow zone is randomly perturbed to provoke transversal instabilities within the detonation front. After a short time period, the solution demonstrates a cellular pattern of the detonation. The simulation continues until the mean propagation velocity and the mean cell size become stable. Numerical soot foils are obtained by recording the maximum pressure history in the laboratory frame of reference.

3. Experimental results

3.1. Shock wave induced detonation onset

As a first step, the evolution of shock velocity as a function of the driver to driven pressure ratio (P_4/P_1) was measured. For this series of experiments, the length of the shock-tube driven section was 3.80 m. Stoichiometric mixtures, diluted with 50 mol% Ar, at initial pressures of 10 kPa and 20 kPa were used. Figure 1 shows the results obtained at initial pressure of 10 kPa. The velocity of the incident shock increases with increasing (P_4/P_1). Up to a ratio of around 50, the measured velocity is in good agreement with the velocity calculated using the shock wave theory as illustrated by the dashed line. At a critical ratio around 52, a sudden increase in wave speed is observed when the coupling between the shock wave and the reaction zone occurs and the combustion emergy release results in a detonation. From the measured shock velocity, around 1100 m/s, the critical post-shock thermodynamic state at this (P_4/P_1) ratio can be calculated. The temperature and

pressure are respectively 904 K and 127 kPa. The critical pressure ratio for detonation onset was found to be substantially lower, $(P_4/P_1)_c = 35$, at an initial pressure of 20 kPa. For these conditions, the critical post-shock thermodynamic state is 750 K and 188 kPa. The decrease of $(P_4/P_1)_c$ is due to the increasing reaction rate with the increase of the pressure.

Figure 2 shows an example of a detonation onset soot record obtained in a rich H_2-N_2O-Ar mixture. In the left part of the foil, a sharp discontinuity can be seen. This may correspond to the collision of the retonation wave with the contact surface. The detonation onset is located between the discontinuity and the first visible detonation cells. Consistent with previous observations on detonation initiation [49, 50], the initially overdriven detonation wave has very small detonation cells and as the detonation velocity decreases toward the Chapman-Jouguet value, the cells increase in size.

3.2. Detonation velocity and cell size

The velocity of the detonation waves and the detonation cell size have been measured over a range of equivalence ratios, dilutions and initial pressures. For this series of experiments, the length of the shock-tube driven section was increased to 4.60 m, in order to ensure that the detonation was not over-driven.

For hydrogen-nitrous oxide mixtures diluted with 40% Ar, Figure 3 , the experimental velocity is slightly lower than the Chapman-Jouguet value with a mean deficit around 2%. The velocity maximum is shifted toward rich mixtures due to the variations in thermochemical properties with composition.

An example of soot record is shown in Figure 4. Cell sizes as a function of the equivalence ratio at different dilutions and initial pressures are shown in

Figure 5 and Figure 6. Only experiments where the detonation waves were self-sustained are considered. The error bars in the figures correspond to the maximum and minimum cell sizes measured. The dependency of the cell size on the equivalence ratio follows the classical U-shaped curve with a minimum for stoichiometric H_2-N_2O mixtures. The cell size decreases with increasing initial pressure and decreasing dilution. These trends are consistent with previous studies on hydrogen-nitrous oxide mitures [38, 39] and trends observed for other mixtures [51].

4. Numerical results

4.1. Kinetic scheme validation and reduction

4.1.1. Kinetic scheme validation

The reaction mechanism was validated against ignition delay times from previous reflected shock wave experiments [20, 21, 23, 24]. Figure 7 shows the experimental results [23, 24] and the model predictions for lean mixtures, 99 mol% diluted with Ar, at reflected shock pressures of 300 kPa and 900 kPa. For the whole set of data (230 points), the mean relative error is 29%, which is on the same order as the experimental uncertainty. Sensitivity analysis shows that the most important reactions involve N_2O and that the reactions, which consume or produce H atoms, are also quite important. This feature can be explained by a reaction pathway analysis. The formation of excited OH radicals, OH*, is achieved according to the following sequence: $N_2O(+M)=N_2+O(+M)$; $O+H_2=OH+H$; $N_2O+H=N_2+OH^*$. The initiation step is the decomposition of N_2O and H atoms and N_2O are the precursors of OH* radicals. Thus reactions that produce and consume H atoms strongly

influence the computed delay time. Moreover, since N_2O is involved in two steps of this sequence, reactions which compete for its consumption are also important, especially the $N_2O+H=N_2+OH$ reaction.

The kinetic model has also been tested against other data from the literature [20, 21]. Ignition delay times obtained by Hidaka from OH* radical profiles are reproduced with a mean error below 15%. Delay times obtained from N_2O decay signal are also shown in Figure 8.

In order to extend the validity of the model to lower temperatures, flow reactor experiments from Allen et al. [52] have been modeled. Figure 9 presents the results obtained. A time shift of 0.064 s has been applied in order to align the experimental and numerical points corresponding to 50% of H_2 consumption. Figure 9 shows that the consumption of N_2O and H_2 as well as the formation of H_2O are reasonably predicted as long as this shift is included.

The detailed model can also be used to predict laminar flame speeds for H_2-N_2O-Ar mixtures as shown in [33, 53]. Through this extensive validation, the present detailed kinetic mechanism for H_2-N_2O mixtures is suitable for the modeling of a wide range of combustion events and initial conditions.

4.1.2. Kinetic scheme reduction

The purpose of the mechanism reduction was to obtain realistic reaction models of small size to describe the reaction kinetics in conditions that are representative of detonation waves. A stoichiometric H_2-N_2O mixture diluted with 40% Ar was considered. Initial temperature and pressure conditions were $T_1 = 295$ K and $P_1 = 10$ kPa. In order to account for the wide range of post-shock states behind cellular detonation fronts, the reduction

was performed on a parametric grid defined in terms of postshock conditions, T_{sh} and P_{sh}, corresponding to 17 equally spaced shock velocities from $0.8D_{CJ}$ to $1.6D_{CJ}$. Depending on D, the postshock conditions vary within the ranges: T_{sh} = 1315-4035 K and P_{sh} = 236-965 kPa.

The automatic procedure described in [54] led to the set of reactions presented in Table 2. It is composed of 11 reversible chemical reactions and 13 species (including Ar). By analyzing the reduced model R1-R11, it was found that the role of the R6-R11 subset essentially consisted in limiting the consumption of H atoms by R5. Reverse reaction R6 constitutes an alternative pathway to R5 and allows the formation of NH, which participates in the following reactions, R7 to R11, involving N_xH_y species. Further reduction could thus be achieved by eliminating reactions R6 to R11 and multiplying the rate constant of reaction R5 by a correction factor α. The relative errors on the time to thermicity peak and the maximum thermicity induced by this modification are shown as a function of α in Figure 10. The best compromise is obtained with $\alpha = 0.56$, leading to $\alpha A_{R5} = 1.24\times10^{14}$ cm^3/mol s. Figure 11 compares the temperature and thermicity profiles in the ZND reaction zone obtained with the detailed, reduced (R1 to R11) and semi-globalized (R1 to αR5) reaction models for the detonation velocity: $D/D_{CJ} = 1$ and 1.3. From this comparison, a reasonable agreement can be seen, which proves that the semi-globalized model describes the overal oxidation process with a good accuracy.

4.2. Numerical simulation

4.2.1. Numerical cell size

Example of experimental and numerical soot foils are shown in Figure 12. They were obtained for a stoichiometric H_2-N_2O mixture with 40% Ar dilution at $T_1 = 295$ K and $P_1 = 10$ kPa. The vertical scale represents the absolute coordinate in the laboratory frame. Comparing the soot foils in Figure 12 (a) and (b), it is observed that the numerical detonation cells are slightly more regular and significantly smaller. The mean width is around 10 mm whereas the experimental mean value is around 17±8 mm. In order to identify the cause of this disagreement, the effect of the detonation velocity on the cell size has been studied. The detonation speed in the experiment was measured at 1860 m/s whereas it is 1910 m/s in the simulation. Based on ZND simulations, a decrease of 75 K of the post-shock temperature, 1788 against 1864 K, and an increase of the induction zone length by 43%, 0.843 against 0.588 mm, are created by such a decrease of wave speed. The velocity deficit of a detonation wave is associated with heat and momentum losses due to the divergence of the stream lines induced by the boundary layer displacement effects and wave curvature [50, 56]. These effects can be taken into account within the framework of a steady one dimensional model by including heat transfer and friction coefficients [57, 58] or a curvature term [59]. For multi-dimensional simulations, detailed consideration of boundary layer and confinement effects have to be accounted for using a highly-resolved viscous model. A simple approach that accounts for the net effect of reduction of the wave speed is to reduce the energy release by the reaction. Such an approach has been previously adopted by Virot et al. [55]. In the present

study, the energy release reduction has been modeled by slightly decreasing the heat of formation of H_2O. Although this approach does not account for the physical mechanism responsible for the energy losses, it enables reproducing the experimentally observed cell size and mean reaction zone length. A more realistic description of energy loss mechanisms in detonation wave is beyond the scope of the present study. Numerical calculations have been performed and it was found that the experimental velocity could be matched in the simulation by changing the H_2O standard enthalpy at 298 K from -241.8 kJ/mol to -221.1 kJ/mol. Figure 12 (c) presents a numerical soot foil obtained after applying this modification. The decrease of the detonation speed by 50 m/s has a drastic effect on the obtained detonation cell width. The mean cell size measured from Figure 12 (c) is around 18 mm and agrees well with the experimental value of 17±8 mm. Simulations were conducted with both a higher spatial resolution or different boundary conditions. The grid size was varied between 100 and 25 μm. Symmetry or periodic conditions were used on the lateral boundaries. The outflow boundary used a Riemann solver to enable the CJ condition to be achieved at some distance away from the outlet boundary. The position of the outlet boundary with respect to the detonation front was also varied. These numerical experiments demonstrated that the computed cell size is effectively independent of these parameters. The observed independence of the cell size on the grid resolution is consistent with the findings of Powers and Paolucci [60] who showed using 1D simulation that the macroscales, i.e. the average induction length, of detonation wave are only slightly modified by increasing resolution. The leading order factor in determining the cell size is the post-shock temperature and

thus the detonation velocity has a the main effect on the cell size.

4.2.2. Detonation front structure

The detonation front structure was studied for nitrogen-diluted H_2-N_2O mixtures in order to perform a comparison with the experimental schlieren and PLIF images of Austin [61]. The semi-globalized reaction model developped for Ar-diluted mixtures proved satisfactory to model N_2-diluted mixture based on ZND calculations and was used without modifications to perform these simulations.

Figure 13 (a) shows an example of instantaneous density gradient field (Schlieren picture) obtained numerically for a H_2-N_2O-1.64N_2 mixture at T_1 = 295 K and P_1 = 20 kPa. The induction zones between the shock and the reaction front (dark regions next to the wave front) are visible. The details of the vortex structures are resolution dependent and will be determined by the numerical viscosity due to the WENO scheme. A more realistic simulation of fine structure of the detonation flow field and reaction zone requires using a viscous model, Navier-Stokes equations, rather than the inviscid Euler model [62]. Powers and Paolucci [60] concluded from 1D simulation results that a submicron mesh would be needed to spatially resolve the smallest gradients for a detonation in a H_2-air mixture at P_1=101 kPa and T_1=298 K. Because the computational time increases with the number of species, Ni, as 2^{Ni}, such a high resolution is extraordinarily difficult to achieve for 2D simulation when including realistic chemistry [63]. Moreover, it is unclear if this level of resolution is helpful for two-dimensional simulation as spatial graidents and diffusive fluxes are most important wihtin regions of high shear, which

require either sub-grid scale models ot three-dimensional simulations. Figure 13 (b) and (c) show experimental schlieren pictures obtained by Austin [61] for H_2-N_2O-1.64N_2 and H_2-N_2O-1.33N_2 at $T_1 = 295$ K and $P_1 = 20$ kPa. Several common features can be seen: (i) the irregular structure of the detonation front, (ii) intense transversal shock waves which are a characteristic of very unstable detonation [61] and (iii) small-scale density fluctuations just behind the detonation front.

To compare the numerical simulation to experimentally observed the reaction zone structures, a Laser Induced Fluorescence (LIF) model has been used to post-process the numerical results. This procedure enables realistic comparison between the simulation and the experimental results from Austin [61]. A complete description of the LIF model can be found in [64, 65]. Briefly, the three-level model of Bessler et al. [66] is used. Laser excitation from the ground state (level 1) to the upper state (level 2) results in fluorescence emission due to transitions from level 2 to all possible vibrational and rotational levels in the electronic ground states (level 3). The contributions of the $A^2\,\Sigma^+ \leftarrow X^2\,\Pi$ (1,0) Q2(8) and $A^2\,\Sigma^+ \leftarrow X^2\,\Pi$ (1,0) Q1(9) absorption lines, at 35210.25 and 35210.68 cm^{-1}, respectively, were taken into account. Figure 14 shows a comparison between experimental and numerical schlieren, PLIF and superimposed schlieren-PLIF images. Initial conditions are: H_2-N_2O-1.64N_2 mixture at $T_1 = 295$ K and $P_1 = 20$ kPa. Reasonable agreement is observed for the overall features of the OH PLIF and superimposed images. The sharp onset and subsequent decay of the fluorescence signal are well predicted. The progressive attenuation of the LIF signal intensity due to the

laser sheet absorption is apparent as a dark strip both in the experimental and numerical PLIF images. Also shown in the bottom part of Figure 14 are the simulated normalized OH mass fraction field and superimposed schlieren and normalized OH mass fraction field. Noticeable differences are observed with respect to the PLIF field. The resolution of the PLIF technique seems limited in terms of OH concentration distribution at the detonation front. The experimental and numerical PLIF images show a much less variation far behind the front, whereas significant spatial variations at the detonation front are seen in the OH mass fraction field. Because of the absorption of the laser sheet as it travels through the detonation front, the pockets with high OH concentration away behind the front cannot be observed using the PLIF technique.

4.2.3. Analysis of velocity oscillations

It is well established that the detonation leading shock exhibits large velocity oscillations within a cell cycle. To investigate this, data points (up to 800) of the instantaneous shock velocity from the simulations have been analyzed as a function of the normalized cell length, L. The points were extracted along the cell centerlines. Each detonation cell has been divided into 20 sections of equal normalized size. Within each section, the mean velocity and the standard deviation has been extracted from the data. Figure 15 shows the evolution of the instantaneous shock velocity within a normalized cell cycle. The mean local velocity is shown as red points with error bars indicating the standard deviation. The blue solid line represents the theoretical Chapman-Jouguet velocity. At the begining of a cell, the leading shock is highly overdriven with normalized velocity as high as $D/D_{CJ} = 1.5$

in average. The velocity decays exponentially along the cell and drops below D_{CJ} around L = 0.5 to reach $D/D_{CJ} = 0.8$ at L = 0.8. Between L = 0.8 and L = 1, the instantaneous velocity is seen to increase very sharply as a consequence of the re-initiation process. The error bars demonstrates that the local velocity exhibits very large fluctuations, up to 27%, during the re-initiation process whereas fluctations during the decay period are relatively small, around 7%.

Figure 16 presents the probability density distribution of the lead shock velocity obtained from the numerical data analysis. The probability density function is skewed with the highest probabilities slightly below the Chapman-Jouguet velocity. The distribution is spread over a large range of velocity extending from $D/D_{CJ} = 0.7$ to $D/D_{CJ} = 1.8$, reflecting the very large velocity oscillations within a cell cycle. Figure 17 shows local, $\Delta L/L = 0.05$, probability density functions of the shock velocity at different cell cycle positions. Throughout the velocity decay period, the local relative frequency distributions demonstrate relatively narrow single-peak shape as seen in Figure 17 (a). At the begining of the re-initiation process, Figure 17 (b), L between 0.8 and 0.9, the distribution is spread over a large range of values although a high probability peak is still observed. At the end of a cell cycle, Figure 17 (c), L = 0.9-1, the distribution is highly non-uniform and spreads over a large range of velocity values.

5. Discussion

5.1. Detonation front structure

Based on soot foil observations, Strehlow [67] and Libouton [68] proposed four classes of detonation: very regular, regular, weakly regular, and irregular. A more reliable method to classify detonation is to use the results of stability analysis. Schultz and Shepherd [69] used the reduced activation energy as a stability characteristic, whereas Ng et al. [70, 71] used a modified version of this parameter, which accounts for the thermicity profile shape in the ZND solution. Two limiting cases can be distinguished: weakly unstable and highly unstable detonation. The shock front of weakly unstable detonation appears as a sharp line with a smooth contour and high regularity. The reaction zone of a weakly unstable detonation appears smooth and continuous and is characterised by "keystone-like" structures [61]. Highly unstable detonations are characterized by large spatial variation of the shock front strength, small scale instabilities, and highly wrinkled reaction zones with areas of low concentration of hydroxyl radical isolated within areas of high concentration [61, 72].

While 2-D numerical simulation of weakly unstable detonations can be performed relatively easily, the simulation of highly unstable detonations is much more challenging. The intrinsic instability of the physical processes and large range of length scales places high demands on the numerical methods. In the present study, a relatively high dilution, no less that 40%, was maintained because the variations of the mean propagation velocity were too large at lower dilution. The comparison of the experimental and numerical schlieren images demonstrates that most of the qualitative characteristics of unstable

detonation shock front can be reasonably well captured by the simulation. Even some of the small scale density gradients observed in the experiments are reproduced in the simulation although these small scale instabilities are more pronounced in the experiments.

The present results point out some important limitations of the simultaneous schlieren-PLIF technique. The spatial resolution of the PLIF imaging system is too low to observe the fine gradients of OH radical concentration at the detonation front. More importantly, the structure of the far flow behind the detonation front cannot be observed because of the strong absorption of the laser sheet at the front. Both experimental and numerical developments are needed to allow for quantitative measurements using the PLIF technique. Experimental efforts should be focused on multi-wavelength and multi-angle measurements whereas simulations could be improved by employing higher resolution, including molecular transport and performing 3-D simulations.

5.2. Detonation cell cycle dynamics

Beginning with Denisov and Troshin [73], a number of experimental studies [74, 75, 76] have demonstrated that the propagation of multi-headed or cellular detonation is pulsative in nature with cyclic oscillations of the detonation front with respect to the mean motion [51]. At the begining of cyclic oscillation cycle or detonation "cell", the leading shock is highly overdriven and closely coupled with the reaction zone. As the shock progresses through the cycle of oscillation, the leading shock decays, causing the decoupling of the shock front and the combustion zone [77]. At the end of the cell, a strong overdriven shock wave is re-initiated by a local explosion induced by the transverse wave collision [78]. All these features can be observed in the

present simulations.

Austin [61] demonstrated through analysis of experimental schlieren movies that the difference between the maximum and minimum velocities within a cell cycle was of 0.16 D_{CJ} and 0.73 D_{CJ} for a $2H_2$-O_2-17Ar mixture and some hydrocarbon based mixtures, respectively. Eckett [79] reported simulated velocity variations from 1.2 D_{CJ} to 0.9 D_{CJ} along a cell. Gamezo et al. [80] studied numerically the effect of the global activation energy of the mixture on the amplitude of velocity oscillations. An increase of the velocity variations with the activation energy has been reported. For a mixture with a reduced activation energy of 7.4, Gamezo observed velocity variations between 0.7 and 1.7 D_{CJ}. The reduced activation energy of the presently studied H_2-N_2O-Ar mixture is around 8.5. In this case, the lead shock velocity ranges between 0.7 and 1.8 D_{CJ}, which is consistent with previous studies. Analysis of the probability density distributions of the lead shock velocity by Shepherd [81] showed that, in the case of highly unstable detonations, the distribution is spread over a wide range of velocity with the highest probabilities significantly below the Chapman-Jouguet value. These findings are in good agreement with the results of Radulescu et al. [82]. In the case of weakly unstable detonations, it was shown [81] that the probability density distribution is much narrower with highest probabilities very close to the CJ velocity. The evolution of the distribution shape with the activation energy of the mixture is consistent with the increase of shock velocity variations previously discussed. The present analysis supports the results of Shepherd [81] and of Radulescu et al. [82] with respect to the probability density distribution shape, position and even probability amplitude. The analysis of local

probability density distribution presented in Figure 17 is to our knowledge, new. Particularly interesting is the transition in the distribution shape from single peak to a broad spectrum during the shock velocity decay period and the re-initiation period, respectively. This feature can be explained by the relative time scale of the two processes. The velocity change as a function of distance is almost 4 times faster between L = 0.8-1 than between L = 0-0.8. The shock decay period extends until approximately L = 0.8. This progressive decay of the leading shock velocity induces a relatively slow change of the thermodynamic conditions. On the other hand, the re-initiation event is very abrupt and extends over a much shorter period. This very high acceleration of the leading shock induces a rapid change of the thermodynamic conditions. Because of the high global activation energy, any slight spatial variation in the shock strength leads to large changes in the energy release rate resulting in the broad shock velocity distribution observed at the end of the cycle [61].

6. Conclusion

In the present study, detonations propagating in H_2-N_2O-diluent mixtures has been experimentally and numerically investigated. It was shown that these mixtures are very sensitive to detonation with a cell size of few millimeters at an initial pressure as low as 35 kPa, which agrees with the results of previous detonation studies. It was also demonstrated that numerical simulations, which include realistic chemical kinetic schemes, are able to reproduce most of the experimental detonation features including the cell size and detonation front structure. Although time consuming, such sim-

ulations allow access to details that are difficult to obtain experimentally. Comparisons of numerical and experimental OH PLIF images were made by constructing synthetic PLIF images. These images demonstrate the important role of the limitations of both experimental and numerical methods. While reasonable qualitative agreement is obtained for the gross features, reproducing the fine structure will require significant advances in technology and computational sophistification.

Acknowledgement

This work was partly supported by the French "Ministère de l'Éducation Nationale, de l'Enseignement Supérieur et de la Recherche". 2D detonation simulations were performed using computational resources of the EPEE Federation of the CNRS and University of Orléans and of the CCSC Computational Center of Région Centre. The authors are grateful to Professor J. M. Austin (Caltech) for allowing the reproduction of her work in figures 13 and 14.

References

[1] S. A. Bryan, C. M. King, L. R. Pederson, T. Am. Nucl. Soc. 81 (1999) 97–99.

[2] S. Javoy, R. Mével, G. Dupré, Chem. Phys. Lett. 500 (2010) 223–228.

[3] R. Mével, S. Javoy, G. Dupré, Proc. Combust. Inst. 33 (2011) 485–492.

[4] H. Mick, P. Roth, J. Phys. Chem. 98 (1994) 5310–5313.

[5] L. Da Silva Zambom, D. G. Lantin, E. Onoda, P. Verdonck, Thin Solid Films 459 (2004) 220–223.

[6] V. I. Babushok, W. Tsang, D. R. Burgess, M. R. Zachariah, Proc. Combust. Inst. 27 (1998) 2431–2439.

[7] A. Kunz, P. Roth, Proc. Combust. Inst. 27 (1998) 261–267.

[8] S. Koda, Prog. Energy Combust. Sci. 18 (1992) 513–528.

[9] L. G. Britton, Plant Oper. Progr. 9 (1990) 16–38.

[10] J. Surugue, Techniques générales du laboratoire de physique, Éditions du Centre National de la Recherche Scientifique, Paris, 1966.

[11] H. A. Strobel, Chemical instrumentation, Addison-Wesley Publishing Company, Inc, Londres, 1960.

[12] J. Monnier, Science et défense 91, Nouvelles avancées scientifiques et techniques., Dunod, France, 1991.

[13] T. Hirano, J. Loss. Prev. Process Indust. 17 (2004) 29–34.

[14] S. B. Dorofeev, V. P. Sidorov, A. E. Dvoinishnikov, Combust. Flame 104 (1996) 95–110.

[15] H. Henrici, S. H. Bauer, J. Chem. Phys. 50 (1969) 1333–1342.

[16] R. I. Soloukhin, Proc. Combust. Inst. 14 (1973) 77–82.

[17] R. I. Soloukhin, P. J. Van Tiggelen, Bull. Soc. Chim. Belg. 78 (1969) 179–189.

[18] A. Borisov, V. Zamanskii, G. Skachkov, Kinet. Katal. 19 (1978) 26–32.

[19] K. Pamidimukkala, G. Skinner, J. Chem. Phys. 76 (1982) 311–315.

[20] Y. Hidaka, H. Takuma, M. Suga, Bull. Chem. Soc. Jpn. 58 (1985) 2911–2916.

[21] Y. Hidaka, H. Takuma, M. Suga, J. Phys. Chem. 89 (1985) 4903–4905.

[22] I. N. Kosarev, S. M. Starikovskaia, A. Yu. Starikovskii, Combust. Flame 151 (2007) 61–73.

[23] R. Mével, F. Lafosse, L. Catoire, N. Chaumeix, G. Dupré, C. E. Paillard, Combust. Sci. Tech. 180 (2008) 1858–1875.

[24] R. Mével, S. Javoy, F. Lafosse, N. Chaumeix, G. Dupré, C.-E. Paillard, Proc. Combust. Inst. 32 (2009) 359–366.

[25] S. Javoy, R. Mével, C. E. Paillard, Int. J. Chem. Kinet. 41 (2009) 357–375.

[26] R. Mével, S. Pichon, L. Catoire, N. Chaumeix, C. E. Paillard, J. E. Shepherd, Proc. Combust. Inst. 34 (2013) 677–684.

[27] W. G. Parker, H. G. Wolfhard, Proc. Combust. Inst. 4 (1953) 420–428.

[28] G. Dixon-Lewis, M. M. Sutton, A. Williams, Combust. Flame 8 (1964) 85–87.

[29] A. Duval, P. J. Van Tiggelen, Bull. Acad. Roy. Belg. 53 (1967) 366–402.

[30] P. Gray, R. Mackinven, D. B. Smith, Combust. Flame 11 (1967) 217–226.

[31] P. Gray, S. Holland, D. B. Smith, Combust. Flame 14 (1970) 361–374.

[32] M. J. Brown, D. B. Smith, Proc. Combust. Inst. 25 (1994) 1011–1018.

[33] R. Mével, F. Lafosse, N. Chaumeix, G. Dupré, C.-E. Paillard, Int. J. Hydrogen Energ. 34 (2009) 9007–9018.

[34] O. A. Powell, P. Papas, C. Dreyer, Combust. Sci. Tech. 181 (2009) 917–936.

[35] S. P. M. Bane, R. Mével, S. A. Coronel, J. E. Shepherd, Int. J. Hydrogen Energ. 36 (2011) 10107–10116.

[36] S. Coronel, R. Mével, S. P. M. Bane, J. E. Shepherd, Proc. Combust. Inst. 34 (2013) 895–902.

[37] B. Zhang, H. D. Ng, R. Mével, J. H. S. Lee, Int. J. Hydrogen Energ. 36 (2011) 5707–5716.

[38] R. Akbar, M. J. Kaneshige, E. Schultz, J. E. Shepherd, Detonations in H_2-N_2O-CH_4-NH_3-O_2-N_2 mixtures, Technical Report FM-97-3, Explosion Dynamics Laboratory, California Institute of Technology, 1997.

[39] U. Pfahl, E. Schultz, J. E. Shepherd, Detonation cell width measurements for H_2-N_2O-N_2-O_2-CH_4-NH_3 mixtures, Technical Report FM-98-5, Graduate Aeronautical Laboratories, California Institute of Technology, 1998.

[40] A. A. Konnov, Detailed reaction mechanism for small hydrocarbons combustion. release 0.5., 2000.

[41] M. A. Mueller, R. A. Yetter, F. L. Dryer, Int. J. Chem. Kinet. 32 (2000) 317–339.

[42] J. M. Hall, E. L. Petersen, Kinetics of OH chemiluminescence in the presence of hydrocarbons, 40^{th} AIAA/ASME/SAE/ASEE Joint Propulsion Conference and Exhibit, (2004).

[43] J. M. Hall, E. L. Petersen, Int. J. Chem. Kinet. 38 (2006) 714–724.

[44] A. E. Lutz, R. J. Kee, A. J. Miller, SENKIN : a fortran program for predicting homogeneous gas phase chemical kinetics with sensitivity analysis, Technical Report Sand87-8248, Sandia International Laboratories, 1992.

[45] R. A. Yetter, F. L. Dryer, H. Rabitz, Combust. Sci. Tech. 79 (1991) 129–140.

[46] D. Davidenko, Contribution au Développement des Outils de Simulation Numérique de la Combustion Supersonique, Ph.D. thesis, Université d'Orléans, 2005.

[47] G.-S. Jiang, C.-W. Shu, J. Comput. Phys. 126 (1996) 202–228.

[48] X. Zhong, J. Comput. Phys. 128 (1996) 19–31.

[49] J. H. S. Lee, I. O. Moen, Prog. Energy Combust. Sci. 6 (1980) 359–389.

[50] J. H. S. Lee, The Detonation Phenomenon, Cambridge University Press, 2008.

[51] J. H. S. Lee, Annu. Rev. Fluid. Mech. 16 (1984) 311–336.

[52] M. T. Allen, R. A. Yetter, F. L. Dryer, Combust. Flame 112 (1998) 302–311.

[53] R. Mével, Etude de mécanismes cinétiques et des propriétés explosives des mélanges hydrogène-protoxyde d'azote et silane-protoxyde d'azote. Application à la sécurité industrielle, Ph.D. thesis, Université d'Orléans, 2009.

[54] D. Davidenko, R. Mével, G. Dupré, Shock Waves 21 (2011) 85–99.

[55] F. Virot B. Khasainov D.. Desbordes H.N. Presles Shock Waves 20 (2009) 457–465

[56] J.A. Fay J. Chem. Phys. 20 (1952) 942–950

[57] N. Tsuboi Y. Morii A.K. Hayashi Proc. Combust. Inst. 34 (2013) 1999 – 2007

[58] S. Kitano M. Fukao A. Susa N. Tsuboi A.K. Hayashi M. Koshi Proc. Combust. Inst. 32 (2009) 2355–2362

[59] A. Camargo H. Ng J. Chao J. Lee Shock Waves 20 2010 499–508

[60] J.M. Powers S. Paolucci AIAA Journal 43 2005

[61] J. M. Austin, The role of instability in gaseous detonation, Ph.D. thesis, California Institute of Technology, 2003.

[62] K. Mazaheri Y. Mahmoudi M. Radulescu Combust. Flame 159 (2012) 2138–2154

[63] J.L. Ziegler Simulations of compressible, diffusive, reactive flows with detailed chemistry using a high-order hybrid WENO-CD scheme, Ph.D. thesis, California Institute of Technology, 2011.

[64] F. Pintgen, Detonation diffraction in mixtures with various degrees of instability, Ph.D. thesis, California Institute of Technology, 2004.

[65] R. Mével, D. Davidenko, J. Austin, F. Pintgen, J. E. Shepherd, Int. J. Hydrogen Energ. 30 (2014) 6044–6060.

[66] G. Bessler, C. Schulz, V. Sick, J. Daily, A versatile modeling tool for nitric oxide LIF spectra, Proceedings of the Third Joint Meeting of the U.S. Sections of the Combustion Institute (2003).

[67] R. Strehlow, Astronautica Acta 14 (1969) 539–548.

[68] J. C. Libouton, A. Jacques, P. J. Van Tiggelen, Colloque International Berthelot-Vieille-Mallard-Le Chatelier 2 (1981) 437–442.

[69] E. Schultz, J. Shepherd, Validation of detailed reaction mechanisms for detonation simulation, Technical Report FM-99-5, GALCIT, 2000.

[70] H. D. Ng, The effect of chemical reaction kinetics on the structure of gaseous detonations, Ph.D. thesis, McGill University, 2005.

[71] H. D. Ng, Y. Ju, J. H. S. Lee, Int. J. Hydrogen Energ. 32 (2007) 93–99.

[72] F. Pintgen, J. M. Austin, J. E. Shepherd, Detonation front structure: Variety and characterisation. Confined Detonations and Pulse Detonation Engines., Torus Press, Moscow, 2003.

[73] Y. N. Denisov, Y. K. Troshin, Proc. Combust. Inst. 8 (1961) 600–610.

[74] R. A. Strehlow, A. J. Crooker, Acta Astronautica 1 (1974) 303–315.

[75] M. Dormal, J. C. Libouton, P. J. Van Tiggelen, Acta Astronautica 6 (1979) 875–884.

[76] P. J. Van Tiggelen, J. C. Libouton, Ann. Phys-Paris 14 (1989) 649–660.

[77] F. Pintgen, Laser-optical visualization of detonation structures., Master's thesis, Technische Universitat Munchen-California Institute of Technology, 2000.

[78] V. V. Mitrofanov, Progr. Astronaut. Aeronaut. 137 (1996) 327–340.

[79] C. A. Eckett, Numerical and analytical studies of the dynamics of gaseous detonations, Ph.D. thesis, California Institute of Technology, 2001.

[80] V. N. Gamezo, D. Desbordes, E. S. Oran, Combust. Flame 116 (1999) 154–165.

[81] J. E. Shepherd, Proc. Combust. Inst. 32 (2009) 83–98.

[82] M. I. Radulescu, G. J. Sharpe, C. K. Law, J. H. S. Lee, J. Fluid Mech. 580 (2007) 31–78.

[83] J. W. Sutherland, J. V. Michael, A. N. Pirraglia, F. L. Nesbitt, R. B. Klemm, Proc. Combust. Inst. 21 (1988) 929–941.

[84] J. V. Michael, J. W. Sutherland, J. Phys. Chem. 92 (1988) 3853–3857.

[85] W. Tsang, R. F. Hampson, J. Phys. Chem. Ref. Data 15 (1986) 1087–1280.

[86] A. P. Zuev, A. Y. Starikovskii, Khim. Fiz. 10 (1991) 52–63.

[87] P. Marshall, T. Ko, A. Fontijn, J. Phys. Chem. 93 (1989) 1922.

[88] J. A. Miller, C. F. Melius, Proc. Combust. Inst. 24 (1992) 719–726.

[89] J. D. Mertens, A. Y. Chang, R. K. Hanson, C. T. Bowman, Int. J. Chem. Kinet. 23 (1991) 173–196.

[90] D. P. Linder, X. Duan, M. Page, J. Phys. Chem. 99 (1995) 11458–11463.

[91] P. Glarborg, K. Dam-Johansen, J. A. Miller, R. J. Kee, M. E. Coltrin, Int. J. Chem. Kinet. 26 (1994) 421–436.

Figure captions

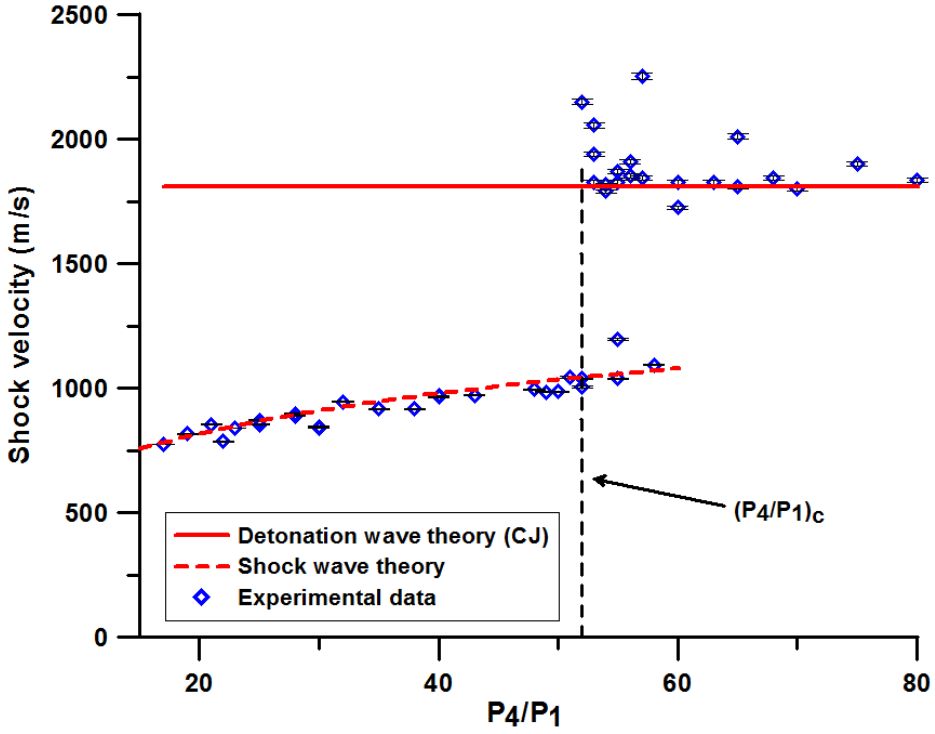
2500
2000
1500
1000
500
0
Shock velocity (m/s)
20
40
60
80
P4/P1
Detonation wave theory (CJ)
Shock wave theory
Experimental data
(P4/P1)c

Figure 1:

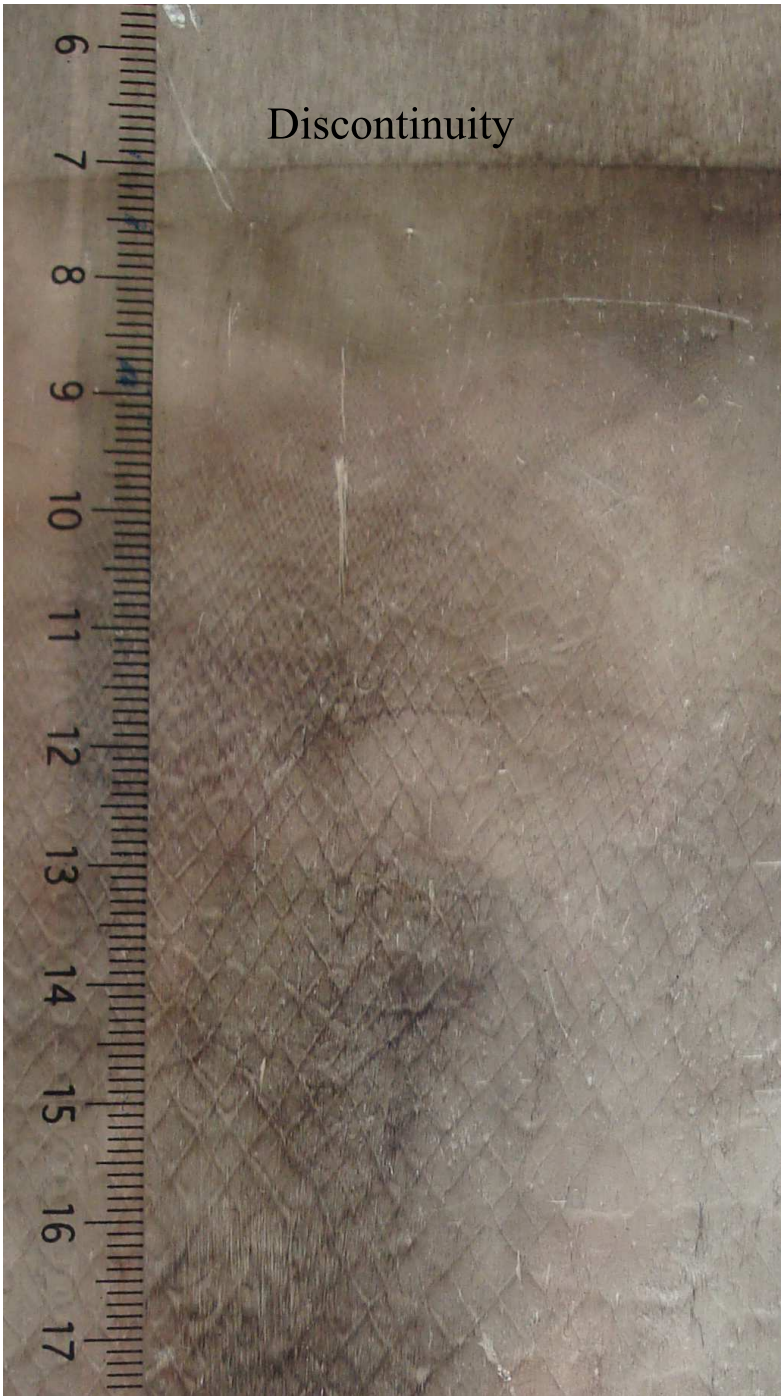

Figure 2:

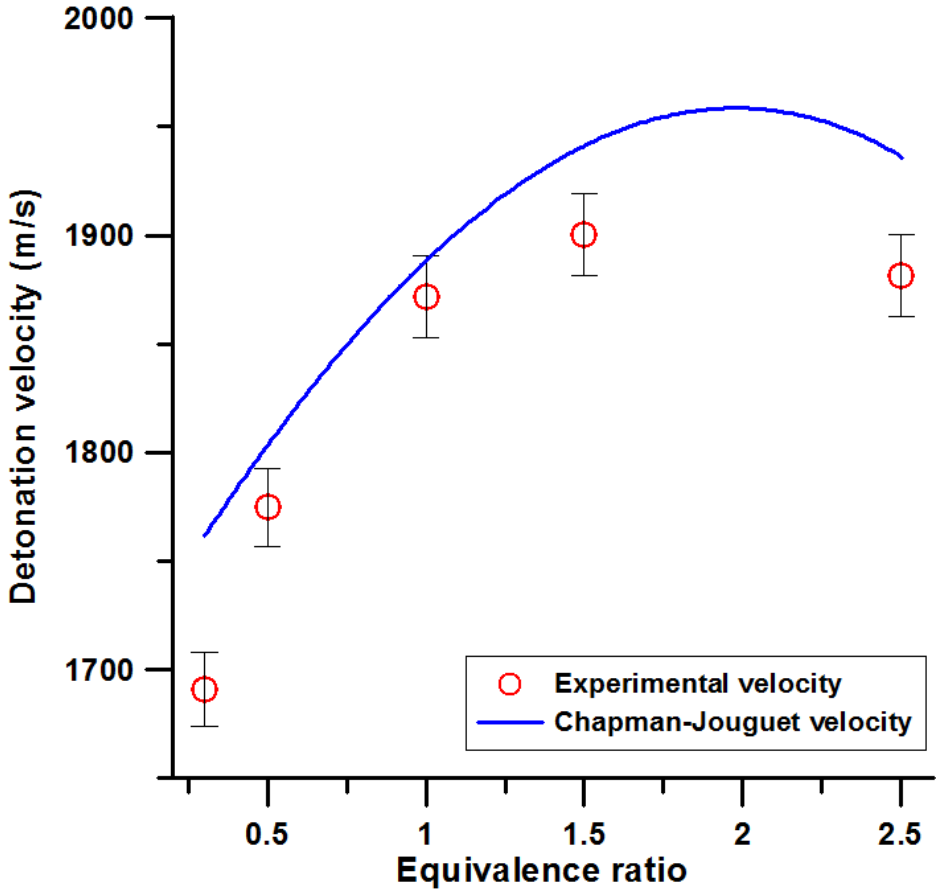
2000
1900
1800
1700
Detonation velocity (m/s)
0.5
1
1.5
2
2.5
Equivalence ratio
Experimental velocity
Chapman-Jouguet velocity

Figure 3:

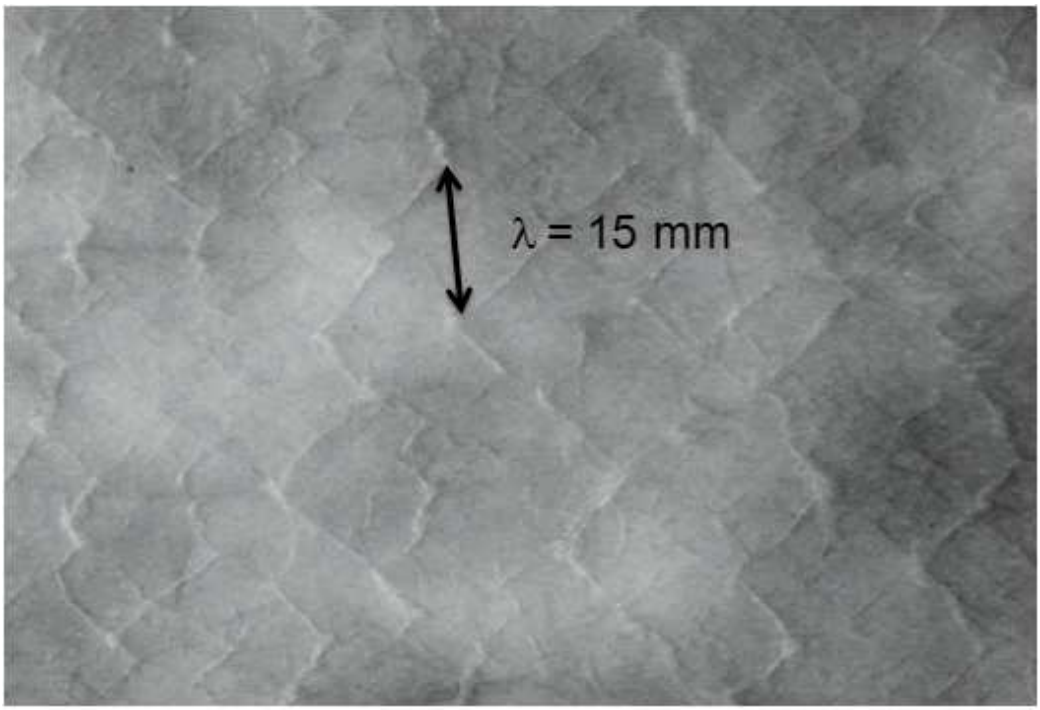

Figure 4:

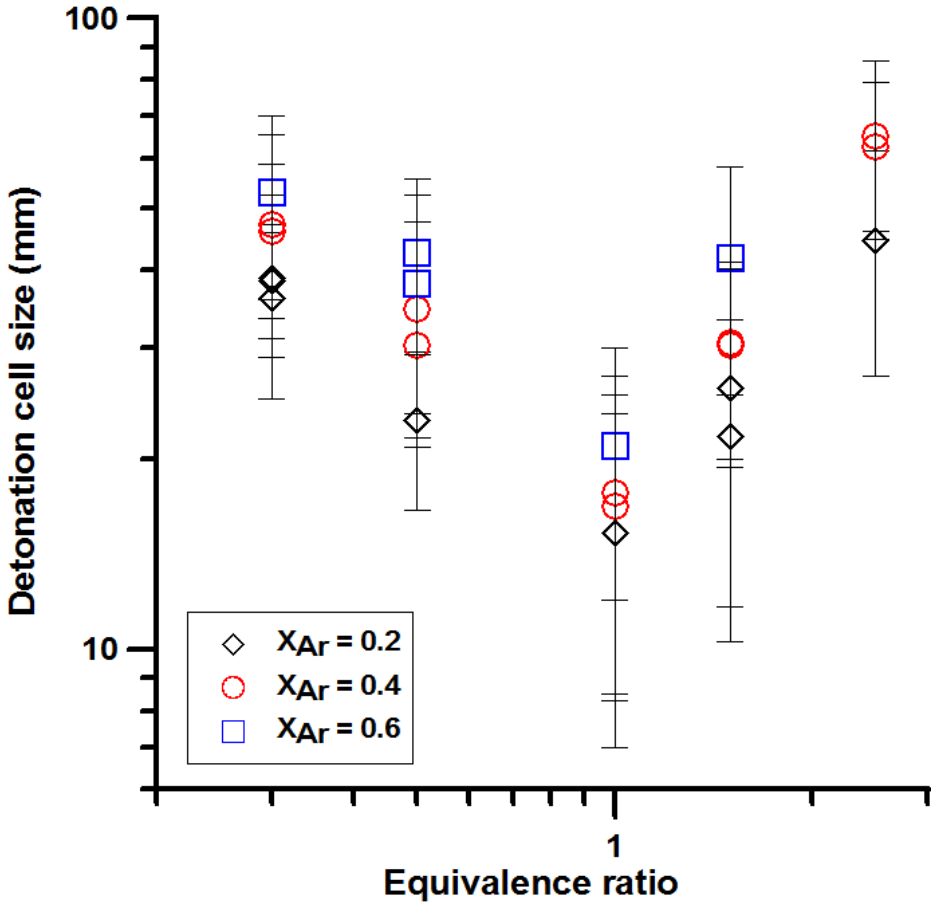
100
10
Detonation cell size (mm)
1
Equivalence ratio
X_{Ar} = 0.2
X_{Ar} = 0.4
X_{Ar} = 0.6

Figure 5:

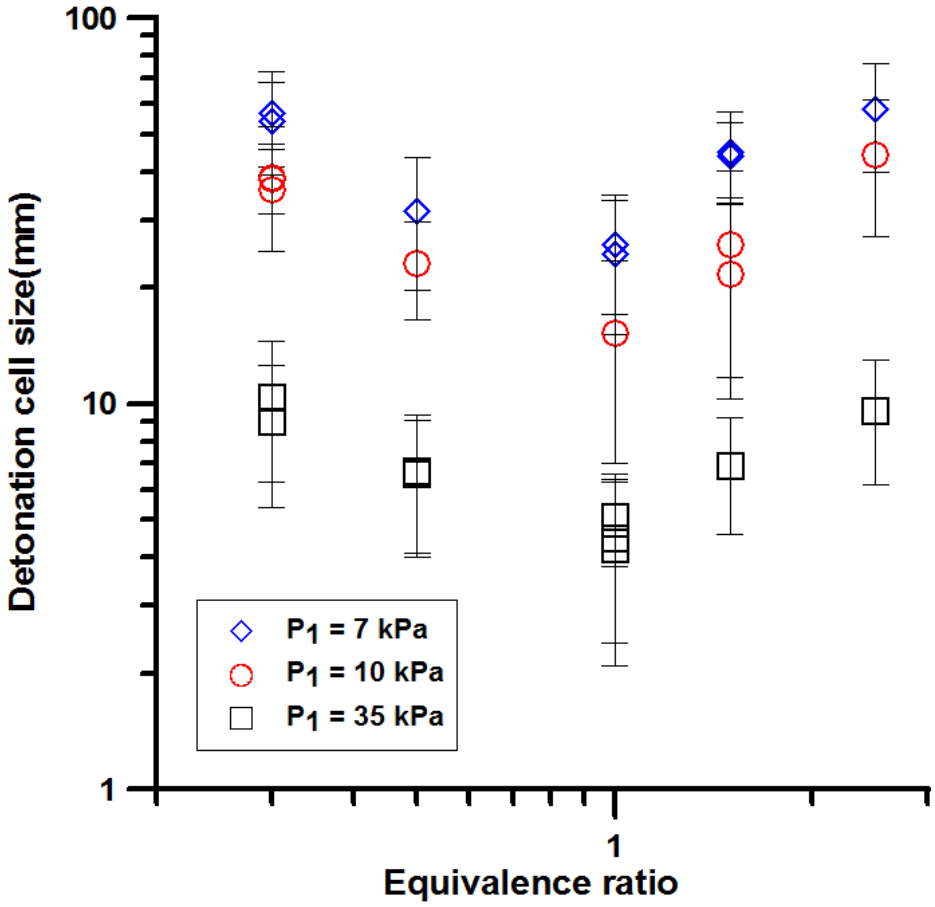
100
10
1
Detonation cell size(mm)
P1 = 7 kPa
P1 = 10 kPa
P1 = 35 kPa
1
Equivalence ratio

Figure 6:

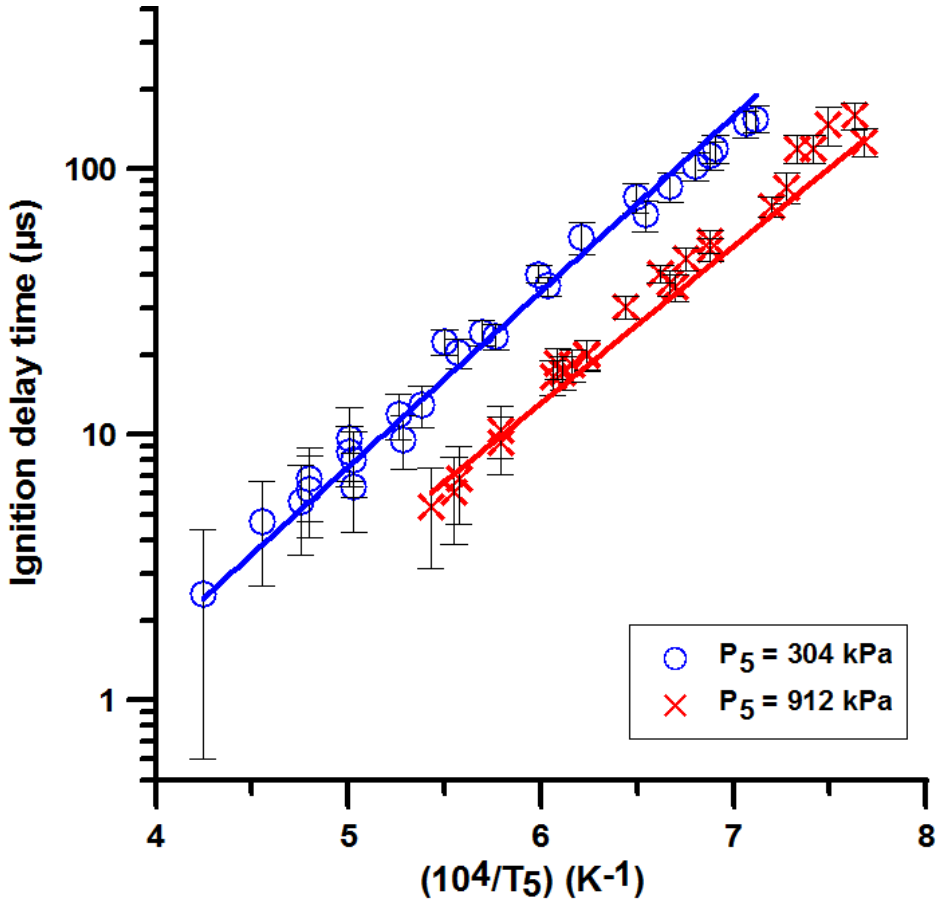
Ignition delay time (μs)
100
10
1
4
5
6
7
8
(10⁴/T5) (K-1)
P5 = 304 kPa
P5 = 912 kPa

Figure 7:

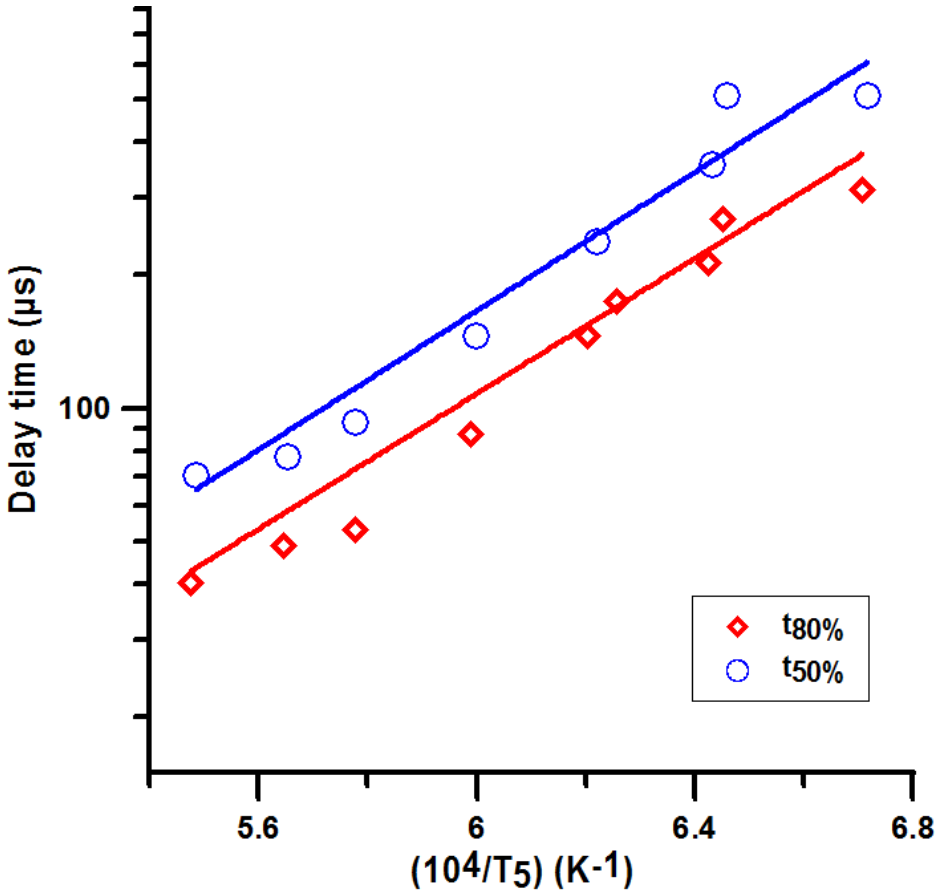

Figure 8:

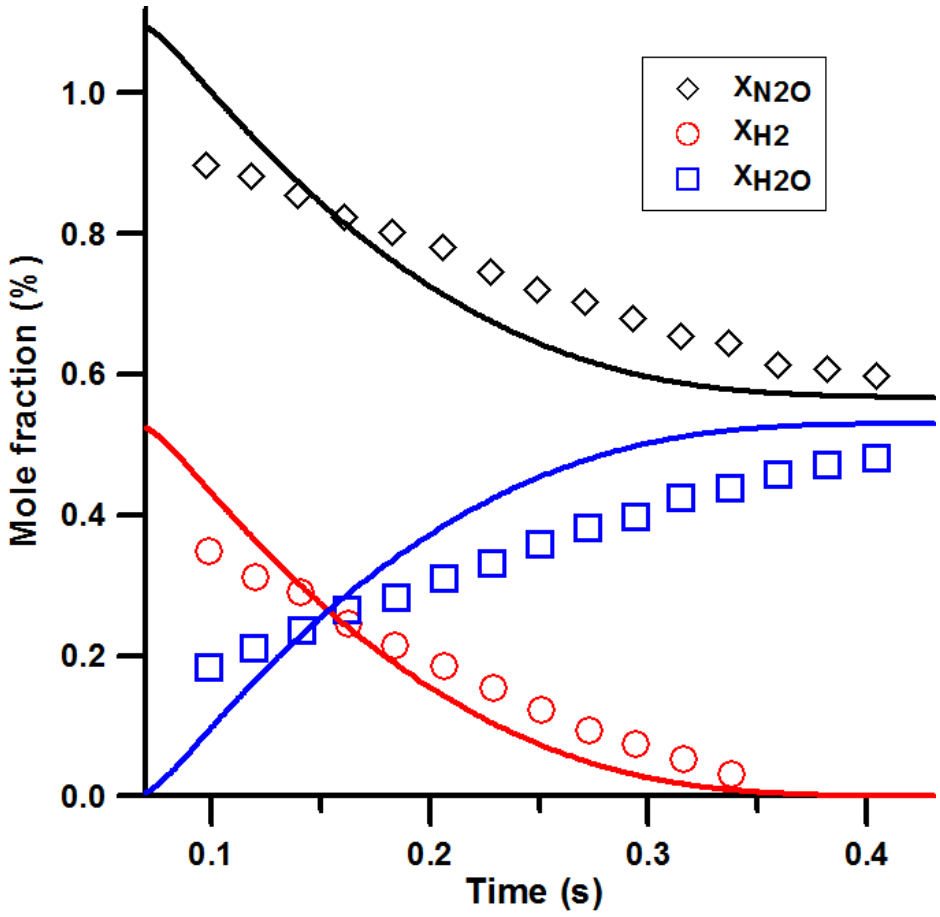

Figure 9:

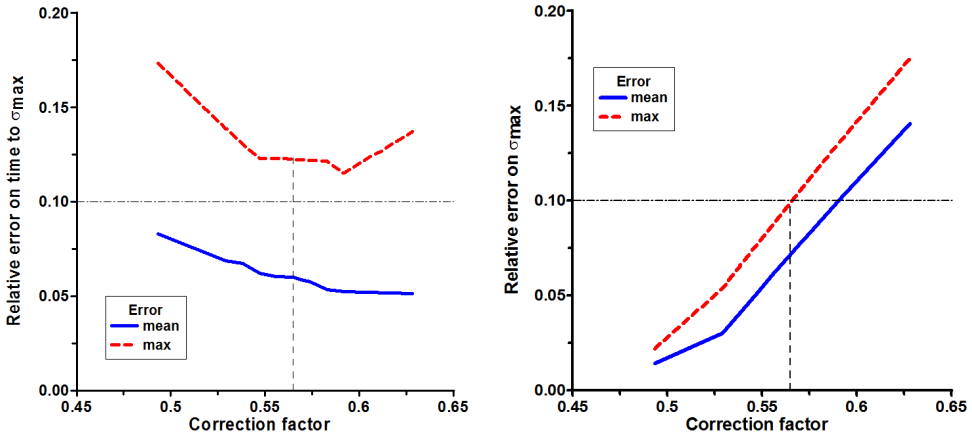
0.20
0.15
0.10
0.05
0.00
0.45
0.5
0.55
0.6
0.65
Relative error on time to σmax
Correction factor
Error
mean
max
Relative error on σmax

(a) (b)

Figure 10:

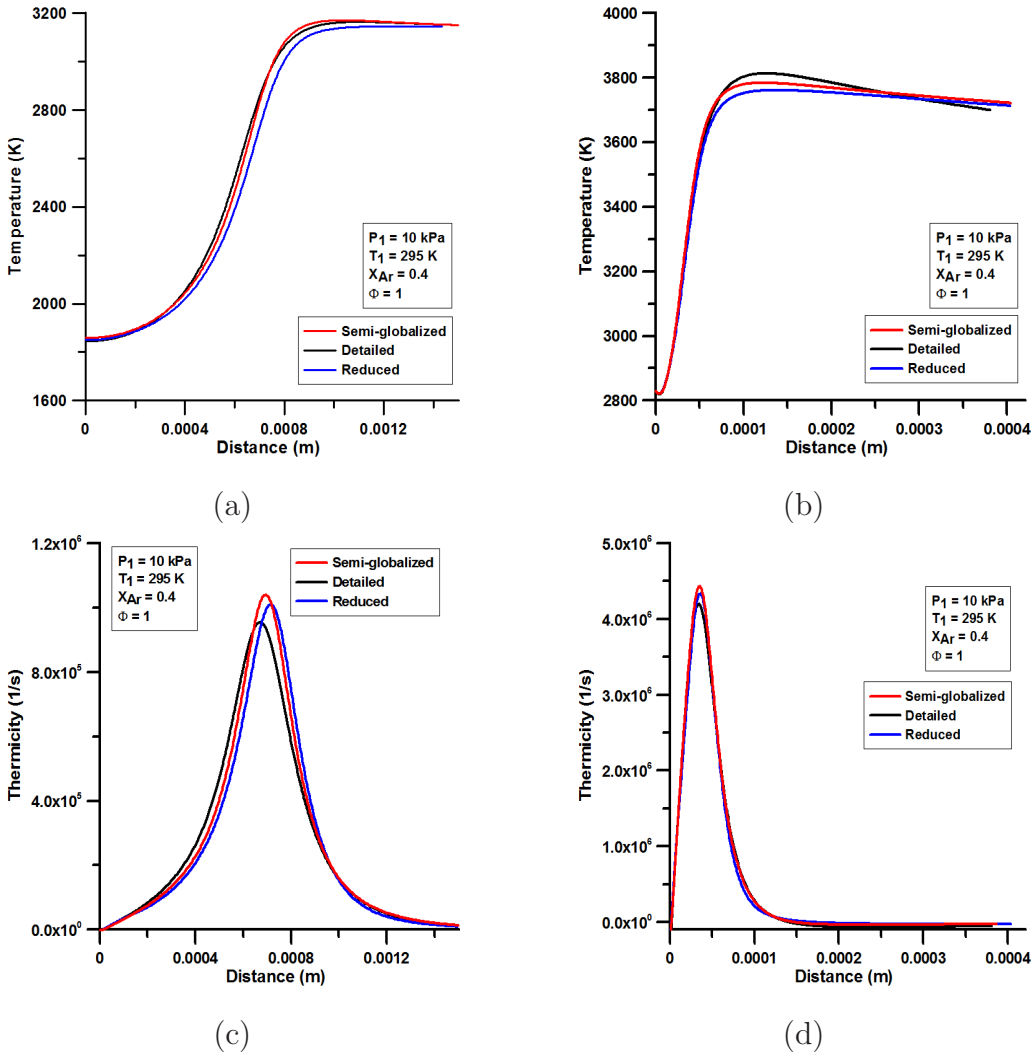
Temperature (K)
Distance (m)
P1 = 10 kPa
T1 = 295 K
XAr = 0.4
Φ = 1
Semi-globalized
Detailed
Reduced
(a)
(b)
Thermicity (1/s)
(c)
(d)

Figure 11:

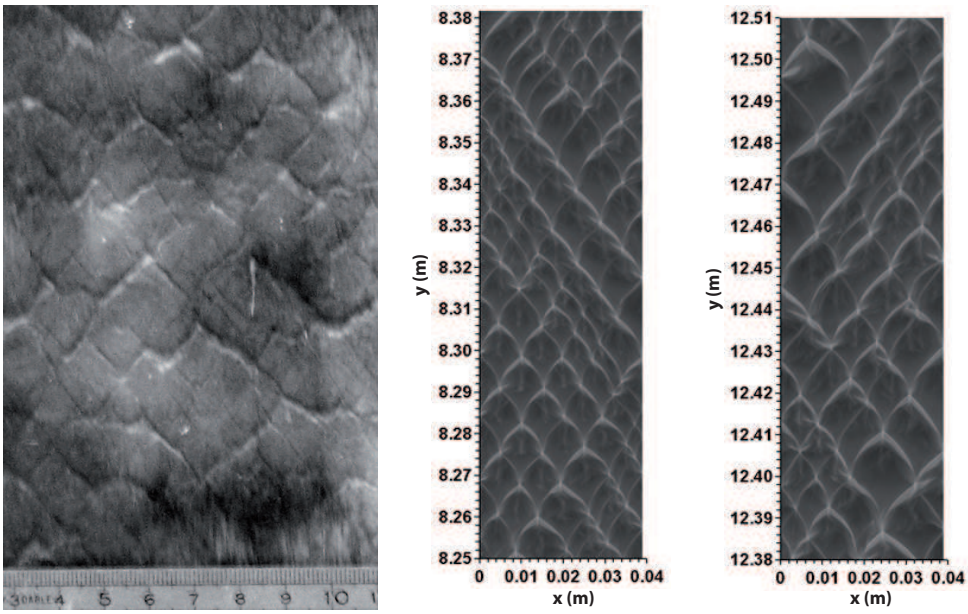

(a) (b) (c)

Figure 12:

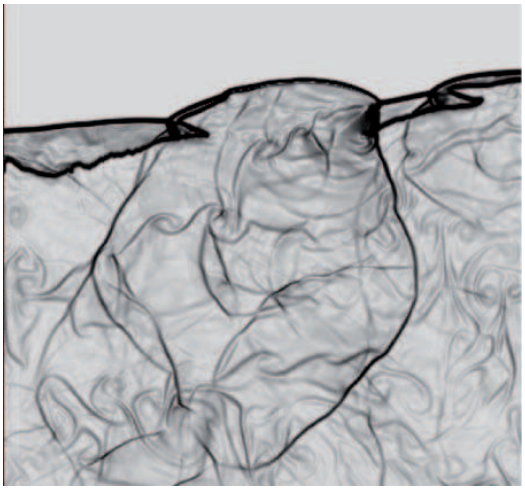

(a)

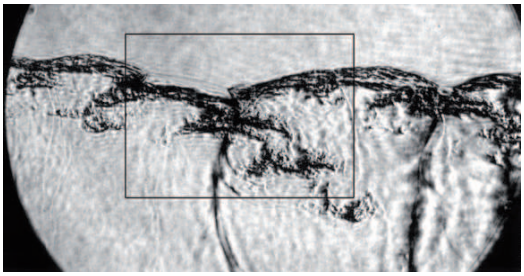

(b)

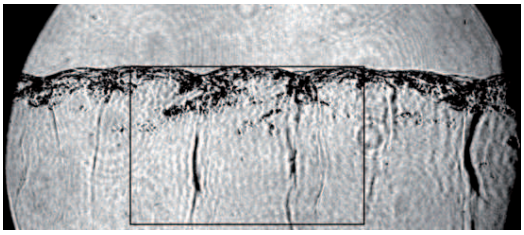

(c)

Figure 13:

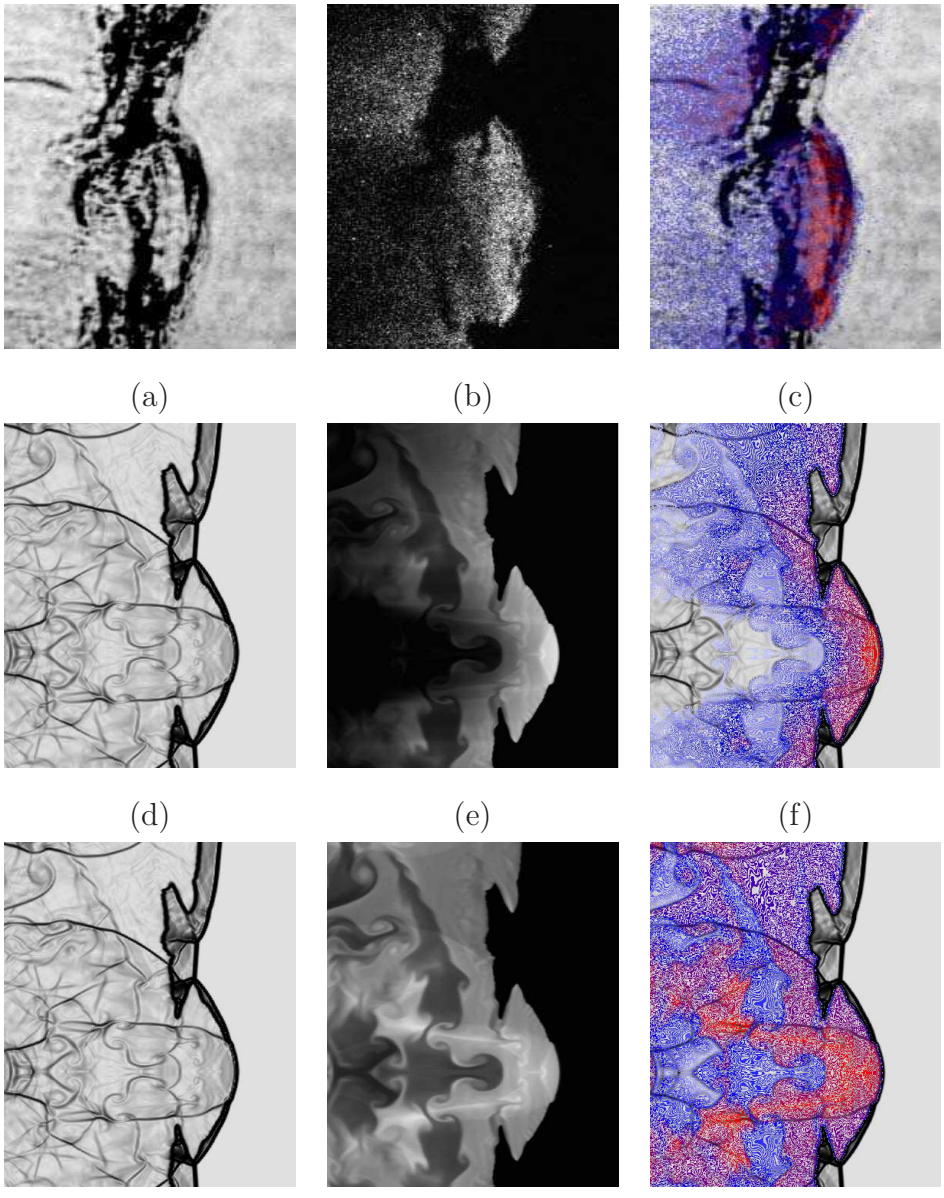

(a) (b) (c)

(d) (e) (f)

(g) (h) (i)

Figure 14:

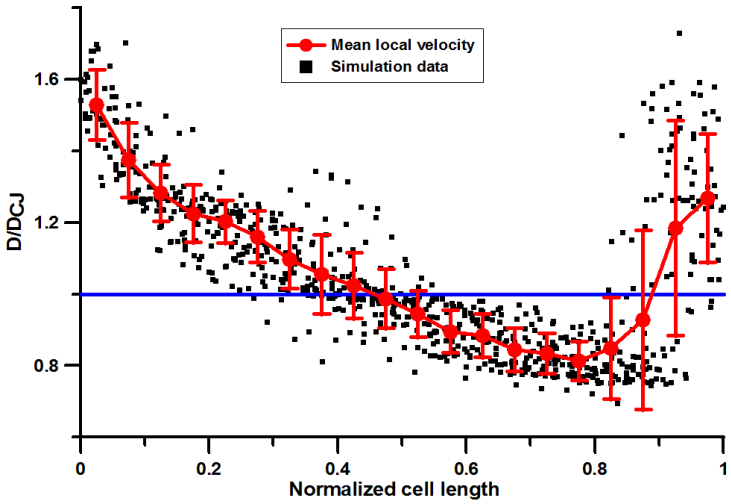
Mean local velocity
Simulation data
D/DCJ
1.6
1.2
0.8
0
0.2
0.4
0.6
0.8
1
Normalized cell length

Figure 15:

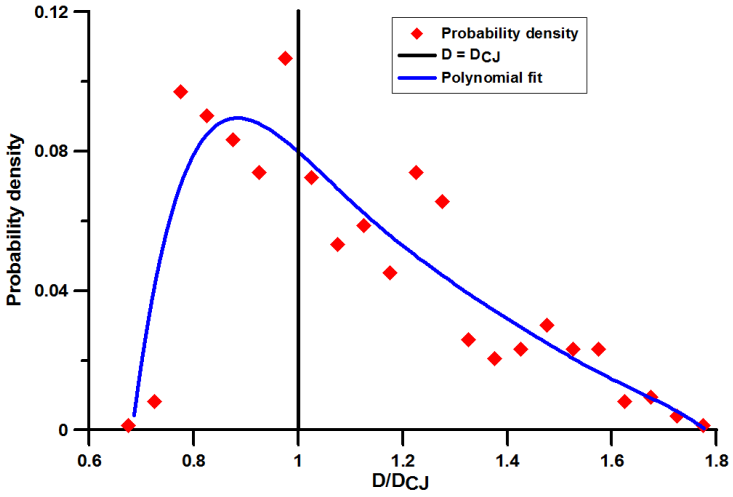
Probability density
D = DCJ
Polynomial fit
Probability density
0.12
0.08
0.04
0
0.6
0.8
1
1.2
1.4
1.6
1.8
D/DCJ

Figure 16:

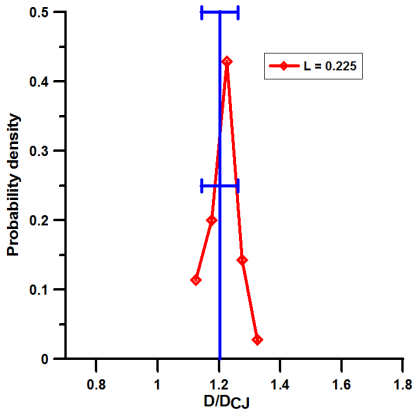

(a)

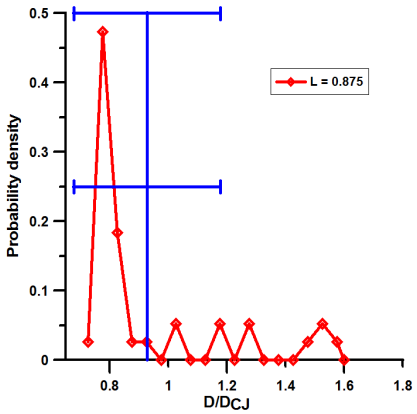

(b)

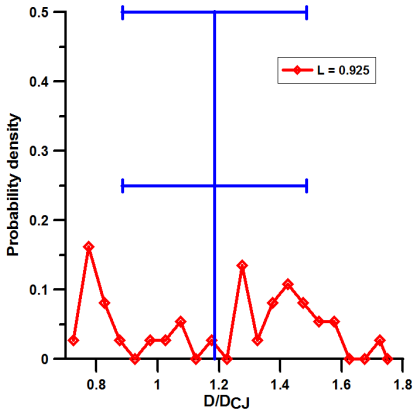

(c)

Figure 17:

Table captions

Table 1: Error criteria for the reduction of detailed kinetic schemes

Parameter	Definition	Error tolerance
Time to peak thermicity	$\delta t_{\sigma_{max}} = \frac{\left\lvert t_{\sigma_{max}} - t^{ref}_{\sigma_{max}} \right\rvert}{t^{ref}_{\sigma_{max}}}$	10 %
Maximum thermicity	$\delta \sigma_{max} = \frac{\left\lvert \sigma_{max} - \sigma^{ref}_{max} \right\rvert}{\sigma^{ref}_{max}}$	10 %
Equilibrium conditions	$\Delta T_{eq} = \left\lvert T_{eq} - T^{ref}_{eq} \right\rvert$	50 K
	$\delta W_{eq} = \frac{\left\lvert W_{eq} - W^{ref}_{eq} \right\rvert}{W^{ref}_{eq}}$	2 %
Temporal profiles	$\delta_{max}\sigma = max\left[\delta\sigma\left(t_n\right)\right]$	15 %
	$\Delta_{max}T = max\left[\Delta T\left(t_n\right)\right]$	150 K
	$\delta_{max}W = max\left[\delta W\left(t_n\right)\right]$	5 %

σ: thermicity, t: time, T: temperature, W: mean molar mass, δ: relative error, Δ: absolute error, max: maximum, eq: equilibrium, ref: reference corresponding to the detailed kinetic scheme.

Table 2:

Number	Reaction	A (cm-mol-s-K)	b	Ea (cal/mol)	Ref
1	$O+H_2=H+OH$	5.08E+04	2.67	6290	[83]
2	$OH+H_2=H_2O+H$	2.16E+08	1.51	3430	[84]
3	$OH+H+M=H_2O+M$	2.21E+22	-2	0	[85]
	Enhanced H_2 = 2.5				
	Enhanced H_2O = 12				
4a	$N_2O=N_2+O$	1.69E+11	0	57653	[86]
4b	$N_2O+M=N_2+O+M$	7.20E+14	0	57410	[25]
	Enhanced N_2 = 1.7				
	Enhanced H_2O = 12				
	Enhanced NO = 3				
	Enhanced N_2O = 3.5				
5	$N_2O+H=N_2+OH$	2.23E+14	0	16750	[87]
6	$NH+NO=N_2O+H$	3.13E+14	-0.45	0	[88]
7	$NH+NH=N_2+H+H$	5.10E+13	0	0	[89]
8	$NH_2+H=NH+H_2$	7.20E+05	2.32	1587	[90]
9	$NH_3+H=NH_2+H_2$	6.40E+05	2.39	10170	[91]
10	$NH_3+NH_2=N_2H_3+H_2$	7.94E+11	0.5	21559	[52]
11	$N_2H_3+M=NH_2+NH+M$	1.00E+16	0	41727	[52]